Ultrasmall 3D network morphologies from biobased sugar–terpenoid hybrid block co-oligomers in the bulk and the thin film states

Chaehun Lee, Brian Ree, Kai Chen, Ryoya Komaki, Satoshi Katsuhara, Takuya Yamamoto, Redouane Borsali, Kenji Tajima, Hsin-Lung Chen, Toshifumi Satoh, et al.

Giant, 17, 2024, 100211

Full-length article

Ultrasmall 3D network morphologies from biobased sugar–terpenoid hybrid block co-oligomers in the bulk and the thin film states

Chaehun Lee[a], Brian J. Ree[b], Kai Chen[c], Ryoya Komaki[a], Satoshi Katsuhara[a], Takuya Yamamoto[d], Redouane Borsali[e], Kenji Tajima[d], Hsin-Lung Chen[c,*], Toshifumi Satoh[d,f,*], Takuya Isono[d,*]

[a] Graduate School of Chemical Sciences and Engineering, Hokkaido University, Kita 13, Nishi 8, Kita-ku, Sapporo, Hokkaido 060-8628, Japan
[b] Department of Chemistry and Physics, Kean University, 1000 Morris Ave, Union, NJ 07083, United States
[c] Department of Chemical Engineering, National Tsing Hua University, Hsinchu 20013, Taiwan
[d] Faculty of Engineering, Hokkaido University, Kita 13, Nishi 8, Kita-ku, Sapporo, Hokkaido 060-8628, Japan
[e] University of Grenoble Alpes, CNRS, CERMAV, 38000 Grenoble, France
[f] List Sustainable Digital Transformation Catalyst Collaboration Research Platform, Institute for Chemical Reaction Design and Discovery, Hokkaido University, Kita 21, Nishi 10, Kita-ku, Sapporo, Hokkaido 001-0021, Japan

Keywords: Block co-oligomer, Saccharide, Terpenoid, Self-assembly, Microphase separation, Ultrasmall nanostructure

Nanoscale three-dimensional (3D) network morphologies, such as those represented by gyroids accessed by the self-assembly of block copolymers, are highly attractive platforms for the fabrication of nanostructured materials. However, it remains challenging to access such morphologies, especially in the sub-10 nm domain spacing region. Herein, we systematically investigated the microphase separation behaviors of biobased sugar–terpenoid hybrid block co-oligomers (BCOs) with different molecular parameters, including their volume fractions, the linker structures between the blocks, and the stereochemistries of the terpenoid blocks. The BCOs were synthesized using the azido–alkyne click reaction of propargyl-β-d-glucopyranoside with azido-functionalized farnesol, phytol, DL-α-tocopherol, and d-α-tocopherol, to ensure a well-defined molecular structure without any molecular weight distribution. Through X-ray scattering screening, we found that tocopherols, when combined with a glucose unit, yield BCOs capable of forming gyroid and hexagonally perforated lamellar (HPL) 3D network morphologies with ultrasmall domain spacings of ~10 nm. Remarkably, HPL, which is known as a metastable phase in block copolymers, was obtained in both the bulk and film states. The nature of the linker structure and the stereochemistry of the tocopherol hydrocarbon chain were found to influence the resulting morphology and the long-range order of the nanostructures. We expect this study to contribute to the molecular design of precise block copolymers and the construction of intricate nanostructural templates with ultrasmall feature sizes.

* Corresponding authors.
E-mail addresses: hlchen@che.nthu.edu.tw (H.-L. Chen), satoh@eng.hokudai.ac.jp (T. Satoh), isono.t@eng.hokudai.ac.jp (T. Isono).
Received 4 September 2023; Received in revised form 13 November 2023; Accepted 19 November 2023

https://doi.org/10.1016/j.giant.2023.100211

Introduction

Block copolymers (BCPs), which consist of two chemically different block chains connected by a covalent bond, self-assemble to form microphase-separated structures with a nanoscale periodicity due to immiscible nature of the two blocks [1–4]. According to the theoretical phase diagram based on the self-consistent field theory, a specific desired morphology can be realized by adjusting the volume fraction (f) and the segregation strength between the constituent blocks given by the product of the Flory–Huggins parameter (χ) and the degree of polymerization (N), i.e., χN. Typical morphologies include lamellae (LAM), hexagonally packed cylinders (HEX), and body-centered cubic (BCC) spheres, and the periodicities of these structures (i.e., their domain spacings, d) are known to range from a few to hundreds of nanometers, depending on the value of N. These nanostructures created by BCP are promising materials for use in various nanofabrication applications. For example, LAM structures vertically aligned to semiconductor substrates can be applied as lithographic masks to fabricate integrated circuits with line-and-space patterns [5–8]. Additionally, vertically aligned HEX structures can be applied as templates for fabricating holes and pillars on a substrate through etching or infiltration processes [9,10].

Among the microphase-separated structures that can be obtained from BCPs, three-dimensional (3D) network morphologies, represented by the bicontinuous double gyroid (GYR) [11–15], bicontinuous double diamond (OBDD) [16–20], hexagonally perforated lamellae (HPL) [14–16,21–25], or the *Fddd* structure [26–29], are particularly attractive in the context of nanofabrication applications. For example, the unique topological structure of the GYR renders it suitable for various use in catalysis [30,31], filtration membranes [32,33], drug carriers [34–36], photovoltaics [28], photonic crystals [37,38], and Weyl materials [39]. More specifically, GYR-, OBDD-, and *Fddd*-forming BCPs containing a selectively degradable block can be utilized to create a nanoporous polymer with a continuous nanochannel, which can be further applied as a template for fabricating nanoporous inorganic materials [28,40–43]. On the other hand, HPL-forming BCP thin films can be utilized as ring-shaped nanotemplates on a substrate, as demonstrated in the fabrication of phase-change memory devices [25,44].

Despite the promising potential of 3D network morphologies in various application fields, the construction of such morphologies is challenging because of their relatively narrow phase window [45]. In addition, the majority of these network morphologies are considered to be metastable and are therefore rarely observed [24,45,46]. Thus, in addition to thorough optimization of the annealing conditions, delicate control of the f and χN values is required to design BCPs that produce the desired morphologies.

An equally difficult challenge in obtaining such a 3D network morphology is the reduction in d to <10 nm. More specifically, the construction of structures with ultrafine d values is essential for achieving high-performance devices that require large specific surface areas. Since the d values of microphase-separated structures are scaled by $N^{2/3}\chi^{1/6}$ in the strong segregation regime, lowering N is an efficient means to reduce d. Nevertheless, microphase separation occurs only when χN exceeds a critical value (e.g., 10.5 for symmetric BCPs), and so the use of high χ and low N BCP systems that combine two low-molecular-weight segments with a large incompatibility is necessary to realize microphase separation with ultrafine d values. Indeed, a number of combinations of different polymers have been reported to realize the concept of high χ–low N BCPs. For example, a BCP comprising polystyrene and poly(4-vinylpyridine)propane-1-sulfonate with a molecular weight of 3.1 kg mol^{-1} yielded the LAM structure with a d value of 5.7 nm [47], and a BCP consisting of polystyrene and polydimethylsiloxane with a molecular weight of 16 kg mol^{-1} generated the HEX structure with a d value of 8 nm [48]. Although a wide variety of high χ–low N BCPs have been reported in the past few years, the majority of resulting morphologies have been limited to the conventional LAM and HEX structures, and only a handful of examples related to the GYR and HPL structures have been demonstrated [47,49–53]. It would therefore be interesting to establish a novel molecular design principle for BCPs to produce a range of 3D network structures with sub-10 nm dimensions.

Saccharide-based high χ–low N BCP systems have been shown to be promising platforms for constructing ultrasmall 3D network morphologies. Previously, our group reported a combination of hydrophilic oligosaccharides and hydrophobic polymers to achieve strong segregation, which enabled the realization of microphase-separated structures with d values as small as ~5 nm. More importantly, our group demonstrated access to the GYR structure with a cubic lattice parameter as small as 12.6 nm (d_{211} = 5.2 nm). This was achieved using low-molecular-weight discrete block co-oligomers (BCOs) combined with hydrophilic oligosaccharides and hydrophobic terpenoid segments [54]. In another study, using several types of saccharide-*b*-polypropylene, Sita et al. obtained HPL structures with long axis periodicities (i.e., ~15 nm) and GYR structures with cubic lattice parameters of 12–14 nm [51]. Moreover, some amphiphilic molecules consisting of sugar headgroup and alkyl chains, known as glycolipid, have been reported to exhibit thermotropic bicontinuous cubic liquid crystalline structures [55,56]. In addition, by optimizing the molecular topology of the oligosaccharide–terpenoid BCOs, HPL and *Fddd* structures were achieved in the bulk state [57]. These earlier works suggest that saccharide-based low-molecular-weight BCPs (or BCOs) should be optimal starting points for exploring the molecular design principle aimed at producing various 3D network structures with ultrasmall periodicities.

Thus, we herein report the microphase separation behavior of discrete linear BCOs consisting of glucose as the hydrophilic saccharide segment and short terpenoids as the hydrophobic segment, to determine the essential molecular parameters for creating ultrasmall network morphologies. For this purpose, farnesol (Far), phytol (Phy), DL-α-tocopherol (DLToc), and d-α-tocopherol (DToc) are selected as the terpenoid blocks for combination with glucose to produce a series of discrete BCOs, namely Glc–hex-Far, Glc–hex-Phy, Glc–hex-DLToc, Glc–hex-DToc, Glc-bz-DLToc, and Glc-bz-DToc (Scheme 1). These terpenoids consist of three or four isoprene units and possess different molecular shapes; thus, precise control of the BCO volume fraction can be achieved. Here, two sets of BCOs with different types of bridging linkers between the blocks (i.e.,

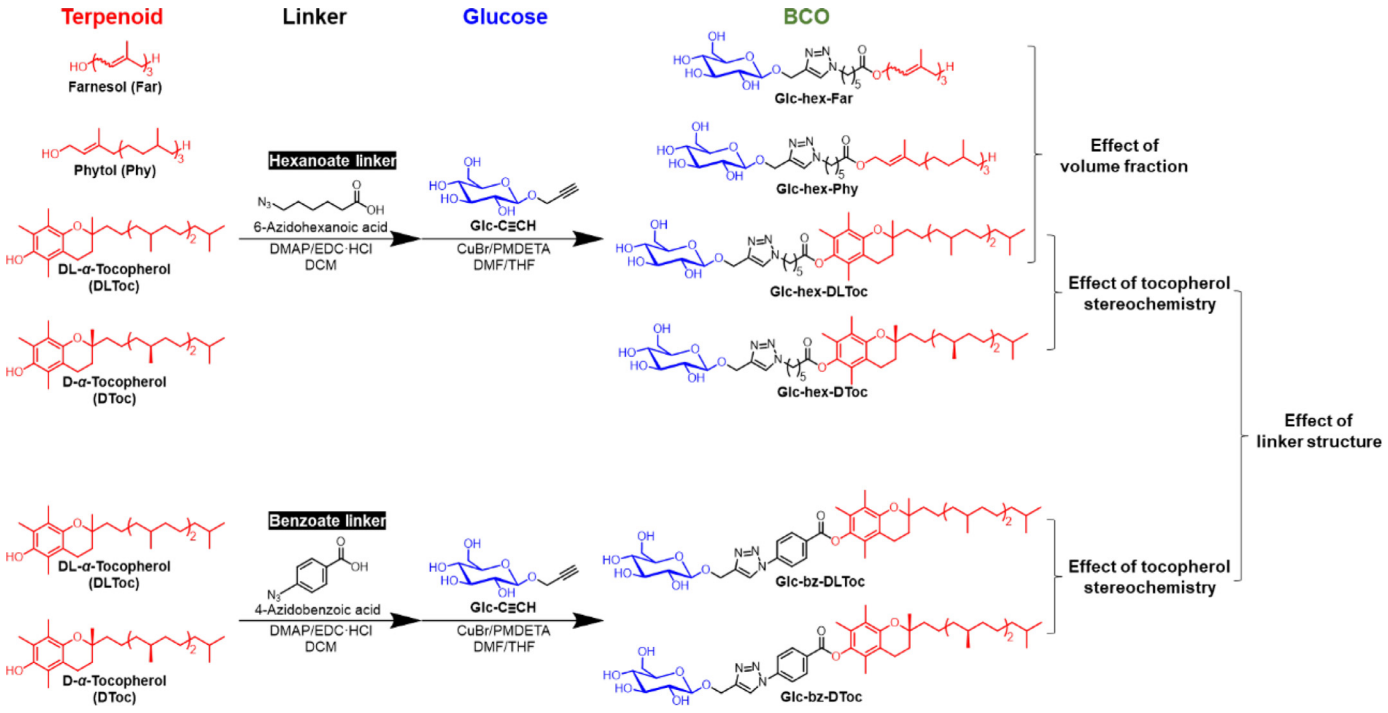

Scheme 1

Synthesis of the sugar–terpenoid BCOs.

hexanoate or benzoate linkers bearing pentylene or phenylene moieties) are synthesized to investigate the effect of the linker structure on the microphase separation behavior. Importantly, the sugar volume fraction (f_{sugar}) is fixed at ~0.3 to ensure the formation of a network morphology. Morphological screening of the bulk state BCOs is then carried out using small-angle X-ray scattering (SAXS) to identify the GYR and HPL structures. Finally, the ability of these BCOs to form stable HPL morphologies in the thin film state is evaluated.

Results and discussion

Initially, the microphase separation behaviors of Glc–hex-Far, Glc–hex-Phy, and Glc–hex-DLToc were investigated in the bulk state to determine a suitable hydrophobic block for constructing 3D network morphologies. Although the synthesis of Glc–hex-Far and Glc–hex-DLToc has been presented in our previous work [54] details regarding their microphase separation behaviors, such as their temperature-dependent morphological changes and order–disorder transitions, have been largely unexplored. Notably, our previous study demonstrated the formation of LAM and GYR structures from Glc–hex-Far and Glc–hex-DLToc, respectively. Thus, in the present study, Glc–hex-Phy-was additionally prepared, which showed a sugar volume fraction in between Glc–hex-Far and Glc–hex-DLToc, and it was expected to provide further details into the phase window. More specifically, Glc–hex-Phy-was synthesized as outlined in Scheme 1. Initially, an azido-functionalized phytol bearing a hexanoate linker (N_3–hex-Phy) was prepared via a condensation reaction between phytol and 6-azidohexanoic acid, and subsequently, this phytol was subjected to a copper-catalyzed azido–alkyne click reaction with propargyl-β-d-glucopyranoside (Glc-C≡CH) to yield Glc–hex-Phy. The success of the click reaction was confirmed by proton nuclear magnetic resonance (^{1}H NMR) spectroscopy, Fourier-transform infrared (FT-IR) spectroscopy, size-exclusion chromatography (SEC), and electrospray ionization mass spectrometry (ESI-MS), as detailed in the Supplementary Material. As a result, the f_{sugar} was calculated to be 0.24 based on $V_{sugar\ segment}/(V_{sugar\ segment} + V_{terpenoid\ segment})$, where V_{sugar} and $V_{terpenoid}$ represent the sugar and terpenoid segment volumes calculated based on known density values. These values are listed in Table 1 together with those of the other BCOs examined herein.

To identify the microphase-separated structures in the bulk state, synchrotron small-angle X-ray scattering (SAXS) and wide-angle X-ray scattering (WAXS) measurements were performed on the as-synthesized and thermally annealed BCOs. In addition, grazing-incidence small-angle X-ray scattering (GISAXS) measurements were conducted to investigate nanostructure formation in the thin film state. Thin film (film thickness: ~40 nm) samples were prepared by spin-coating a 1 wt% polymer solution in tetrahydrofuran (THF) onto a cleaned silicon wafer at 3000 rpm for 1 min. The bulk and thin film samples were annealed at temperatures above the glass transition temperature of the glucose block ($T_{g,sugar}$) and below the 5 % weight loss temperature (T_d) for 6 h under vacuum conditions (see Table 1 and **Figures S13,14** in the Supplementary Material for the determination of $T_{g,sugar}$, and T_d).

Among the various BCOs, Glc–hex-Far and Glc–hex-Phy-were found to exhibit only the LAM morphology in the bulk state, as judged from their SAXS profiles. As shown in Figs. 1a and 2a, Glc–hex-Far and Glc–hex-Phy-exhibited sharp scattering peaks in their SAXS profiles, indicating the formation of highly ordered nanostructures. No obvious scattering peaks were observed in the

Table 1

Molecular characteristics and thermal properties of the BCOs.

BCO	M.W.	$M_{n,SEC}$ [a]	f_{sugar} [b]	f_{ter} [b]	$T_{g,sugar}$ [c] (°C)	T_d [d] (°C)
Glc–hex-Far	580	1500	0.29	0.71	24.0	215.6
Glc–hex-Phy	654	1700	0.24	0.76	26.0	247.8
Glc–hex-DLToc	788	1800	0.21	0.79	39.4	305.4
Glc–hex-DToc	788	1900	0.21	0.79	39.9	310.8
Glc-bz-DLToc	793	1900	0.21	0.79	31.5	272.8
Glc-bz-DToc	793	2000	0.21	0.79	38.0	310.5

[a] Number-average molecular weight determined by SEC in DMF (containing 0.01 M LiCl) with polystyrene calibration.
[b] Sugar and terpenoid volume fractions (f_{sugar} and f_{ter}, respectively) calculated based on the known density values of glucose (1.36 g cm^{-3}), farnesol (0.887 g cm^{-3}), phytol (0.850 g cm^{-3}), and tocopherol (0.950 g cm^{-3}).
[c] Determined by DSC.
[d] 5 % Weight loss temperature (T_d) determined using TGA.

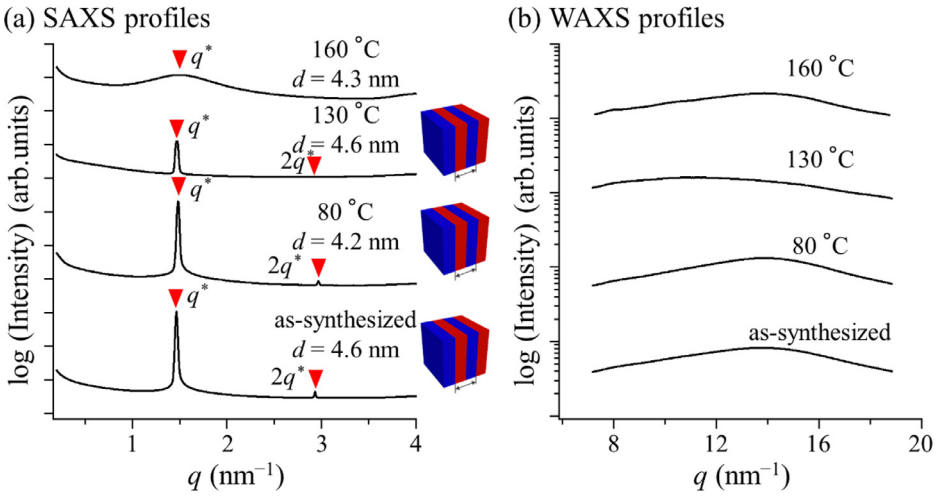

Fig. 1

(a) SAXS and (b) WAXS profiles of the as-synthesized and thermally annealed Glc–hex-Far.

WAXS profiles of Glc–hex-Far and Glc–hex-Phy, either with or without annealing, thereby confirming their amorphous natures (Figs. 1b and 2b). In terms of the thermal analysis results obtained by differential scanning calorimetry (DSC) for Glc–hex-Far and Glc–hex-Phy, heat capacity jumps were observed corresponding to the glass transition of the sugar blocks at $T_{g,sugar}$ (24–26 °C). However, no first-order transitions, such as crystallization, were observed (**Figures S13a,13b**), thereby supporting the WAXS results. As evidenced by the sharp primary peak (q^*) and an additional secondary peak at the $2q^*$ position (Figs. 1a and 2a), Glc–hex-Far and Glc–hex-Phy-formed LAM morphologies without thermal annealing. In the case of Glc–hex-Far, the primary peak became slightly broader upon elevating the annealing temperature, and disorder was observed upon annealing at 160 °C. These analyses suggest that the order–disorder transition temperature (T_{ODT}) is located between 130 and 160 °C. In contrast, Glc–hex-Phy-exhibited sharp scattering peaks associated with the LAM morphology even after annealing at 160 °C. Structurally, the only difference between Glc–hex-Far and Glc–hex-Phy-is the number of isoprene units in the terpenoid block; phytol consists of four isoprene units, whereas farnesol is composed of three isoprene units. It was therefore clear that an increase in the degree of polymerization by one repeating unit significantly affects the thermodynamic stability of the microphase-separated structure. It was deduced that the domain spacing ($d = 2\pi/q^*$) for the 80 °C-annealed Glc–hex-Far was 4.2 nm, which is the smallest value reported to date among sugar-based AB linear BCOs (Fig. 1a) [54]; the d value for 80 °C-annealed Glc–hex-Phy-was slightly larger, i.e., 5.1 nm (Fig. 2a). Notably, control over the d value to a precision of 1 nm was achieved by simply increasing the number of isoprene units in the terpenoid segment.

The thin films generated from Glc–hex-Far and Glc–hex-Phy-also exhibited LAM morphologies, as evidenced by the GISAXS results. In addition, it was found that the two-dimensional (2D) scattering pattern of the as-cast Glc–hex-Far film exhibited a diffraction spot derived from the (100) diffraction of the LAM structure parallel to the Si substrate (Fig. 3a). To determine the structure in greater detail, the one-dimensional (1D) out-of-plane scattering profile was extracted from the 2D scattering image at $2\theta_f = 0.08°$ (Fig. 3b). Subsequently, the d value of the LAM structure was calculated to be 4.4 nm using Bragg's equation ($d = \lambda/(2\sin(\alpha_f/2))$) based on the peak observed at $\alpha_f = 1.62°$ in the out-of-plane scattering profile. As with the d value in the bulk state, this d value was also the smallest reported to date for sugar-based linear AB-BCPs. Furthermore, it was found that the as-cast Glc–hex-Phy-thin film also exhibited a LAM structure parallel to

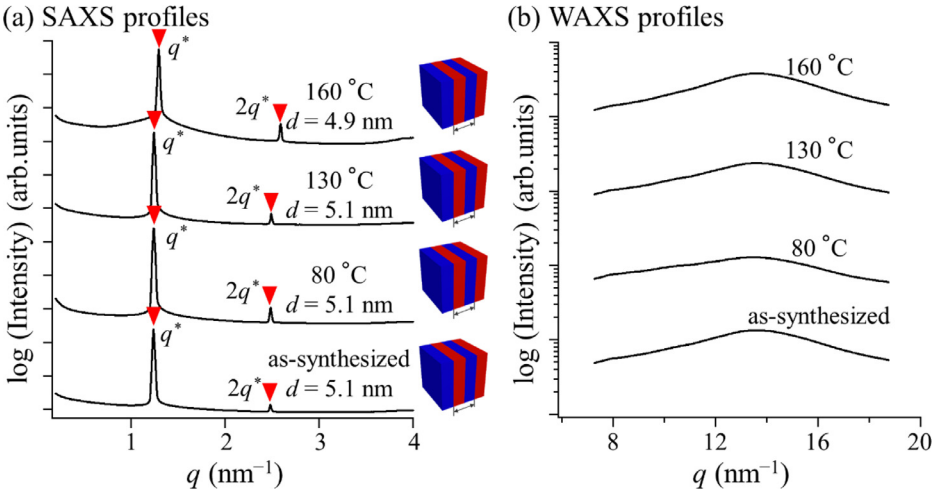

Fig. 2

(a) SAXS and (b) WAXS profiles of the as-synthesized and thermally annealed Glc–hex-Phy.

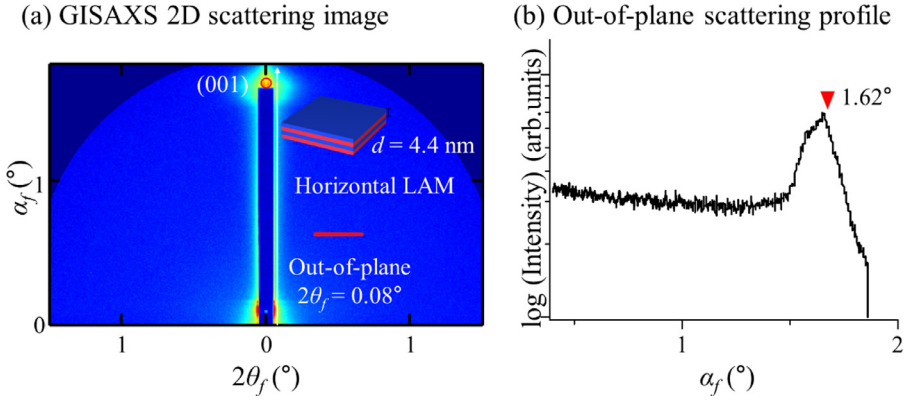

Fig. 3

(a) Representative GISAXS 2D scattering image of the as-cast nanoscale Glc–hex-Far film (40–50 nm thick) with an incidence angle (α_i) = 0.09676°, a sample to detector distance (SDD) = 2947.16 mm, and an X-ray wavelength (λ) = 1.23 Å. (b) 1D out-of-plane scattering profile along the meridian line at $2\theta_f$ = 0.08°, as derived from (a).

the substrate, as evidenced by the diffraction peak observed in the out-of-plane direction (Fig. 4a). The out-of-plane scattering profile was extracted at $2\theta_f = 0.28°$, and a d value of 4.9 nm was calculated using the scattering peak at $\alpha_f = 1.75°$ (Fig. 4b). The above results collectively indicate that farnesol and phytol are the optimal candidates for building blocks to realize ultrasmall d values. However, these BCOs are not suitable for combination with glucose to construct network morphologies.

Subsequently, the combination of glucose and tocopherol was considered to assess the suitability of this BCO for generating a 3D network morphology. Previously, our group determined the potential of Glc–hex-DLToc to form a GYR structure under certain annealing conditions [54]. In the current study, the microphase-separated structure of bulk Glc–hex-DLToc samples was re-investigated under different annealing conditions. The SAXS profile of the as-synthesized Glc–hex-DLToc sample exhibited scattering peaks at q = 0.91, 1.16, 1.44, 1.83, and 3.47 nm^{-1}, which were indexed to the (101), (003), (110), (113), and (009) crystallographic planes of the *ABCABC*-stacked HPL (HPL$_{ABC}$) structure with the $R\bar{3}m$ space group (Fig. 5a and f). The lattice parameters were calculated to be $a = 1/(3(1/d_{101}{}^2 - 1/c^2)/4)^{1/2} = 8.8$ nm and $c = 3(d_{003}) = 16.2$ nm, where a and $c/3$ correspond to the interperforation distance and the lamellar stacking periodicity, respectively. Upon thermal annealing at 80 °C, the scattering peaks became significantly sharper, and the peaks at q = 1.05, 1.17, 1.24, 1.67, 2.02, 2.33, and 3.50 nm^{-1} were assigned to the (101), (003), (102), (110), (113), (006), and (009) reflection planes of the HPL$_{ABC}$ structure with a = 7.4 nm and c = 16.1 nm. A further increase in the annealing temperature resulted in an order–order transition from the HPL$_{ABC}$ to the GYR structure. The scattering peaks observed in the Glc–hex-DLToc samples annealed at 130 and 160 °C appeared at q/q^* = $\sqrt{6}$, $\sqrt{8}$, $\sqrt{16}$, $\sqrt{20}$, $\sqrt{22}$, and $\sqrt{24}$, and were assignable to the (211), (220), (321), (400), (420), and (332) reflection planes of GYR, respectively. The lattice constant a_{GYR} = 12.1 nm was calculated as follows: $a = 2\pi(h^2 + k^2 + l^2)^{1/2}/q_{hkl}$.

Notably, Glc–hex-DLToc was found to form a network morphology, while Glc–hex-Phy-formed only the LAM

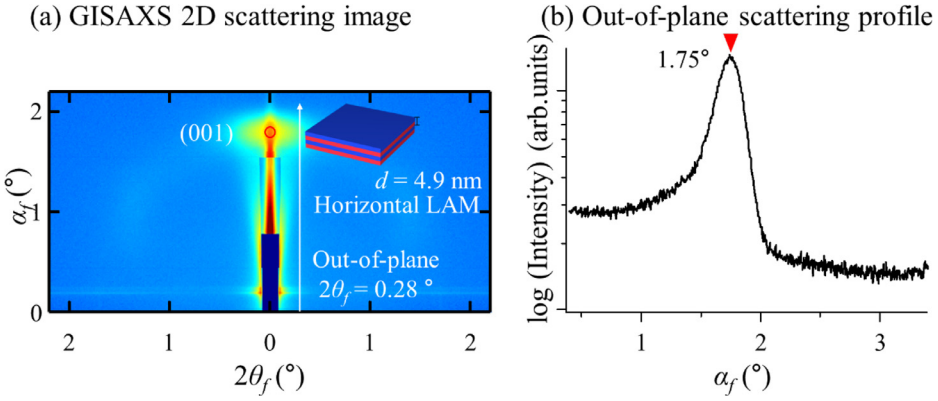

Fig. 4

(a) Representative GISAXS 2D scattering image of the as-cast nanoscale Glc–hex-Phy-film (40–50 nm thick) with $\alpha_i = 0.1512°$; SDD = 2038.91 mm, and $\lambda = 1.50$ Å. (b) 1D out-of-plane scattering profile along the meridian line at $2\theta_f = 0.28°$, as derived from (a).

morphology, despite both BCOs possessing a terpenoid block consisting of four isoprene units. This implies that the molecular shape of the BCO plays a significant role in determining the resulting structure. Similar to the case of micelle-forming surfactants, it is proposed that the packing parameter that characterizes the geometry of the BCO molecule governs the interfacial curvature of the microphase-separated morphology. The packing parameter (P) of a sugar-based BCO is given by $P = v/al_c$, where v is the hydrocarbon volume of the hydrophobic block, a is the effective projection area of the Glc block, and l_c represents the length of the hydrophobic block [58]. It is known that an amphiphilic molecule with a large P value adopts a cone-shaped geometry and tends to form a microphase-separated structure with a larger interfacial curvature, and vice versa. Comparison of the chemical structures of the DLToc and Phy-blocks shows that DLToc contains an additional phenylene ring and a cyclic ether moiety, which effectively increases the hydrocarbon volume of DLToc relative to that of Phy. As a result, Glc–hex-DLToc exhibits a larger packing parameter than Glc–hex-Phy, ultimately favoring the formation of an HPL phase with a larger interfacial curvature than the LAM phase. Thus, Glc–hex-DLToc is a suitable candidate for the formation of ultrasmall network morphologies.

Here, it would be interesting to compare the self-assembly behaviors of the BCOs with chemically similar synthetic glycolipids. Fig. 6 summarizes the phase behaviors of our BCOs, which consist of a glucose unit and terpenoid chain with varied length, together with typical synthetic glycolipids, which consist of a glucose unit (β-anomer) and linear C12, C16, and C18 alkyl chain. There have been many studies on the lyotropic liquid crystalline behaviors of glycolipids [59–61]. However, research into thermotropic liquid crystalline behaviors has only been pursed relatively recently [55,62,63]. Glycolipids typically crystallize at low temperatures. However, above the melting temperature (T_m) of the alkyl chain and below the clearing temperature (T_c) where hydrogen bonds in the sugar moiety are broken, the glycolipids adopt periodic nanostructures in the liquid crystalline state. The strong interaction between the glucose units through the hydrogen bonding is the dominant factor for the self-assembly, resulting in the liquid crystal formation. In contrast, our BCOs show the f_{sugar} of 0.3 or lower, and thus the interaction between the glucose units should have a relatively minor impact on the self-assembly compared to the case of the glycolipids. Therefore, the BCOs are more likely self-assembled into the periodic nanostructures through microphase separation driven by the immiscibility between the glucose unit and hydrocarbon chain. Another indication that our BCOs exhibit microphase separation behavior is their volume-fraction-dependent phase behavior reminiscent of conventional BCP. However, as pointed out by Meijer, BCP-like small molecules can exhibit both liquid crystalline and microphase separation behaviors depending on the delicate balance between directional interaction and immiscibility [64]. Our BCOs may also serve as a bridge between these liquid crystalline and BCP behaviors. This aspect is an interesting topic for further investigation.

These promising results inspired the subsequent combination of tocopherol and glucose to construct an ultrafine network morphology. It should be noted here that the Glc–hex-DLToc species discussed thus far is derived from the synthetic DL-α-tocopherol, and so the stereochemistry of the three stereocenters on the hydrocarbon chain is classed as all-racemic. To gain insight into the impact of the chirality of the terpenoid segment on network formation, an optically pure version of Glc–hex-DLToc was prepared (i.e., Glc–hex-DToc) using natural d-α-tocopherol with an all-(R) configuration (Scheme 1). Similar to its racemic counterpart, the WAXS results for Glc–hex-DToc revealed its completely amorphous nature (Fig. 5b and d). To evaluate the bulk state morphology, SAXS measurements were carried out on the as-synthesized sample and on the specimens annealed at 80, 130, and 160 °C (Fig. 5c). The morphology and unit cell parameters under each annealing condition were found to be the same as those obtained for Glc–hex-DLToc, implying that the chirality of the tocopherol segment has little to no impact on the bulk state self-assembly, and that the microphase-separated morphology seems to be mainly determined by the polar–nonpolar repulsion between the Glc and tocopherol blocks. However, the sharpness of the scattering peaks, which is related to the grain size of the ordered structure, was apparently different

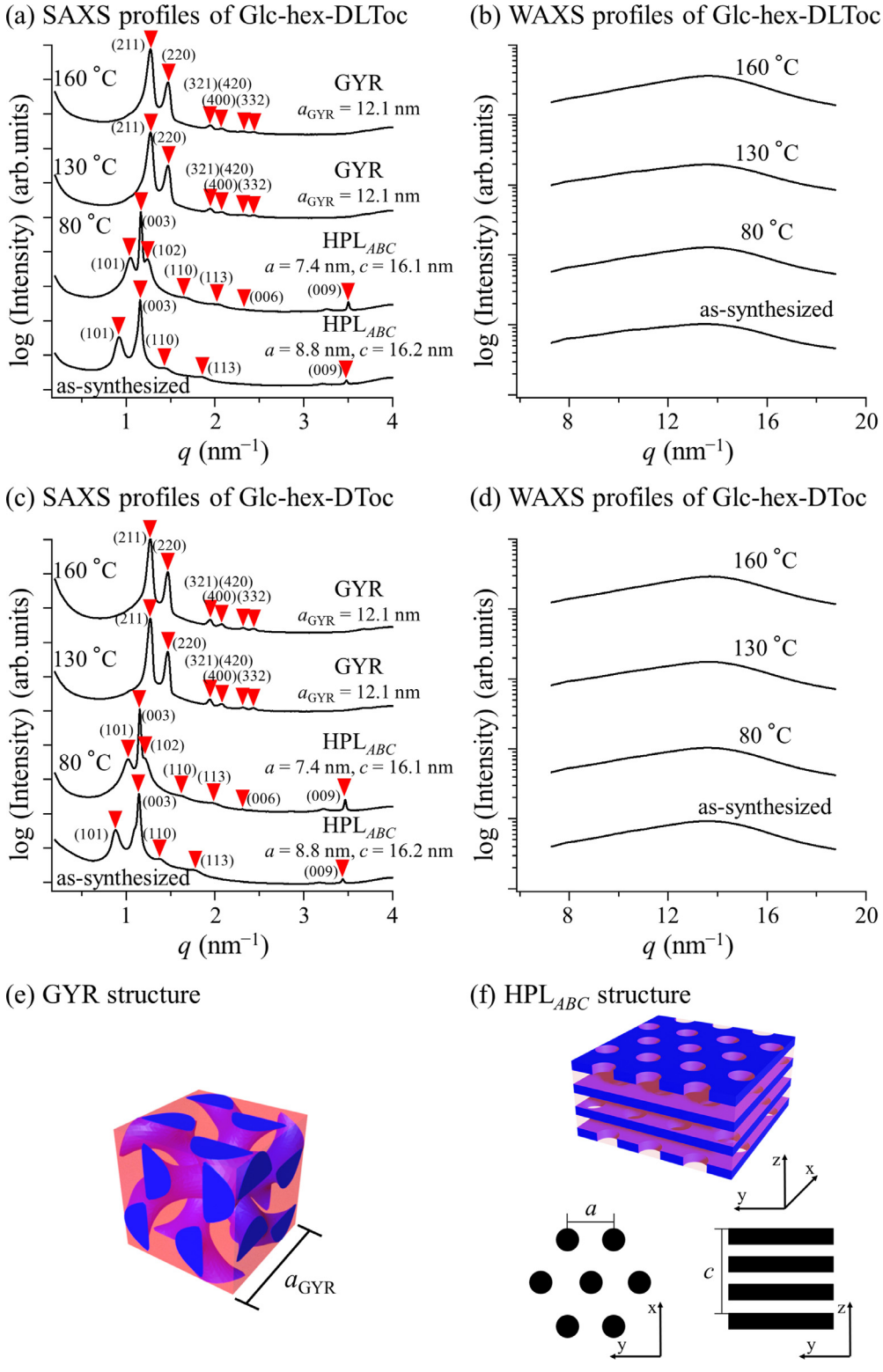

Fig. 5

(a, c) SAXS and (b, d) WAXS profiles of the as-synthesized and thermally annealed Glc–hex-DLToc and Glc–hex-DToc specimens. Also shown are schematic illustrations of the (e) GYR and (f) HPL$_{ABC}$ structures.

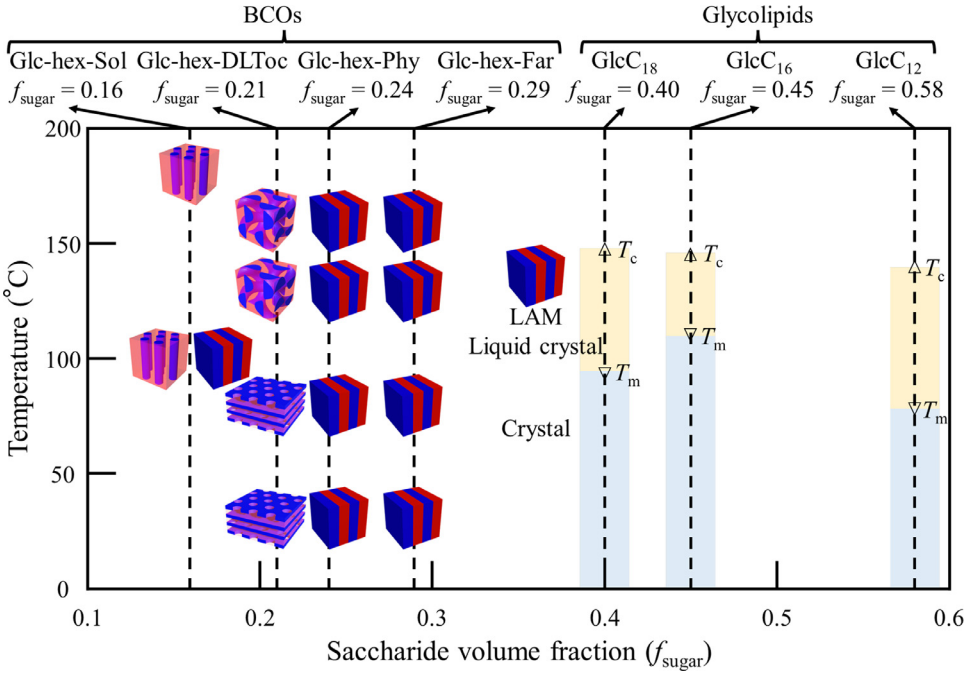

Fig. 6

Phase diagram of Glc–hex-Sol (the "Sol" represents solanesol as the terpenoid block) [54], Glc–hex-DLToc, Glc–hex-Phy, Glc–hex-Far, and typical synthetic glycolipids [55,65–67]. The melting and clearing temperatures are indicated as T_m and T_c, respectively. The vertical axis for the BCOs indicates the annealing temperature.

between the racemic and optically pure BCOs. Thus, to clarify the subtle differences in the nanostructures of Glc–hex-DLToc and Glc–hex-DToc, the primary scattering peaks of the SAXS profiles recorded for the samples annealed at 130 °C were fitted using the Gaussian function to calculate the full width at half maximum (FWHM) (**Figure S15**). As a result, the FWHM values of Glc–hex-DLToc and Glc–hex-DToc were found to be 0.04044 and 0.03525 nm^{-1}, respectively. According to the Scherrer equation ($\tau = K\lambda/\beta\cos\theta$, where τ is the grain size, K is the shape factor, λ is the X-ray wavelength, β is the FWHM, and θ is the incidence angle), the FWHM is inversely proportional to the grain size, and so it can be considered that the GYR structure of Glc–hex-DToc possesses a grain size that is 1.15 times larger than that of Glc–hex-DLToc. Therefore, optically pure tocopherol has an advantage over racemic tocopherol in forming a network morphology with a superior long-range order.

GISAXS experiments were then conducted on thin films of Glc–hex-DLToc and Glc–hex-DToc to investigate the possibility of constructing 3D network structures, and to further clarify the effect of the tocopherol chirality on self-assembly in the thin film state. As presented in Fig. 7a and b, the 2D GISAXS pattern of the as-cast Glc–hex-DLToc thin film shows scattering spots corresponding to the (003), (009), (100), (110), (101), (102), and (108) planes of the HPL_{ABC} structure. The out-of-plane scattering profile extracted from the meridian line at $2\theta_f = 0.24°$ showed two scattering peaks at $\sigma_f = 1.58°$ and 4.79°, corresponding to the (003) and (009) diffractions of the lamellar stacking of HPL_{ABC} parallel to the Si substrate (Fig. 7c). Based on the position of the (003) peak, the d value was calculated to be 5.4 nm. This value correlates to one-third of the repeating length of the *ABC* lamellar stacking; therefore, c was determined to be 16.2 nm. In addition, the 1D in-plane scattering profile extracted from the equatorial line at $\sigma_f = 0.18°$ showed peaks corresponding to the (100) and (110) planes at $2\theta_f = 1.10$ and 1.92°, respectively (Fig. 7d). The positions of these two in-plane peaks led to an a value of 9.0 nm, which represents the distance between the perforations in the HPL_{ABC} structure. Since the GISAXS 2D scattering image recorded for the as-cast Glc–hex-DToc film showed scattering spots at similar positions to those associated with Glc–hex-DLToc (Fig. 8a,c and d), it was considered that Glc–hex-DToc also formed the HPL_{ABC} morphology in the thin film state, with $a = 8.8$ nm and $c = 16.2$ nm (Fig. 8b). However, the Glc–hex-DToc thin film exhibited stronger and sharper scattering spots. In addition, higher-order scattering spots, such as those corresponding to the (104), (107), and (113) planes, were clearly observed (Fig. 8a). These results clearly show that the optically pure Glc–hex-DToc is arranged in a more ordered manner than the racemic Glc–hex-DLToc, even in the thin film state. The HPL_{ABC} structures formed by Glc–hex-DLToc and Glc–hex-DToc in the thin film state can be constructed by spin-coating and can be maintained at a high annealing temperature of up to 180 °C (**Figure S16**). Meanwhile, the long-term stability of the HPL_{ABC} structures in the thin film state is also important for various applications. Thus, we performed GISAXS measurement at one-month intervals for the same thin film samples stored at ambient condition. Comparing the GISAXS 2D scattering images, the HPL_{ABC} structures were found to be maintained over the period of one month, supporting the long-term stability (**Figures S16,17**). Therefore, Glc–hex-

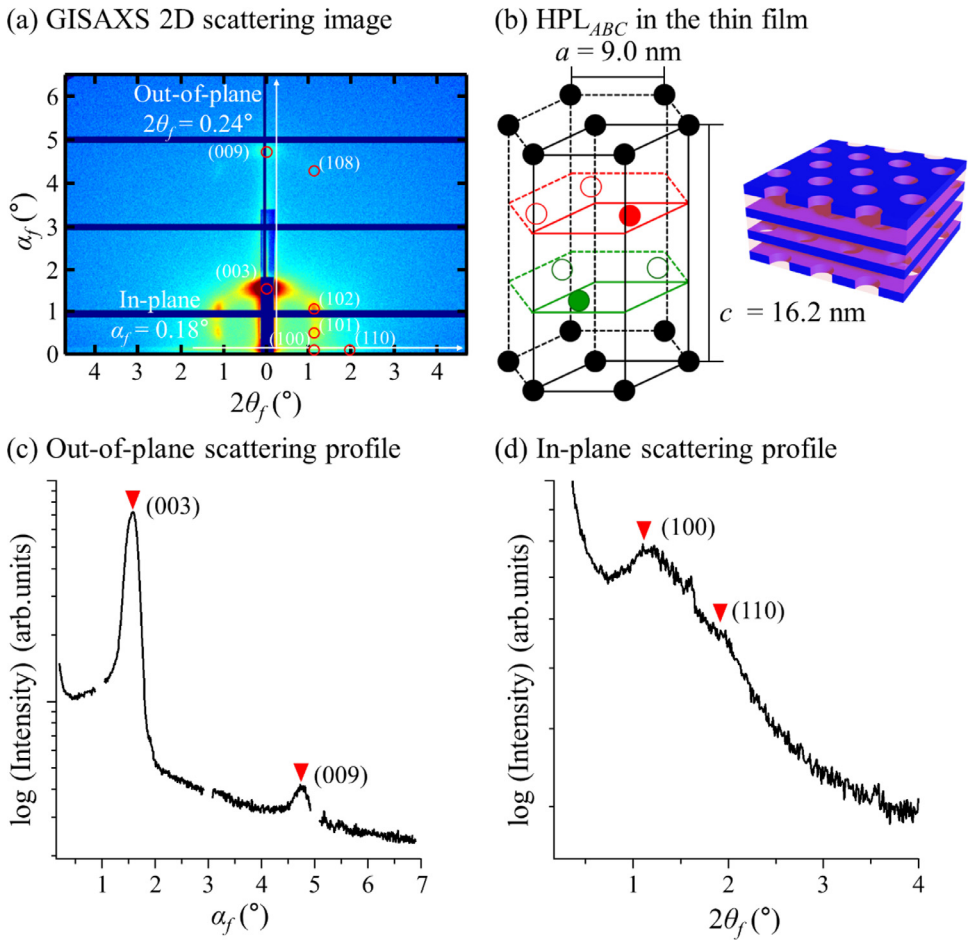

Fig. 7

(a) Representative GISAXS 2D scattering image of the as-cast nanoscale Glc–hex-DLToc film (40–50 nm thick) with $\alpha_i = 0.1803°$, SDD = 1024.29 mm, and $\lambda = 1.50$ Å. (b) Schematic illustrations showing the HPL_{ABC} structure. (c) 1D out-of-plane scattering profile along the meridian line at $2\theta_f = 0.24°$, as determined from (a). (d) 1D in-plane scattering profile along the equatorial line at $\alpha_f = 0.18°$, as determined from (a).

DLToc and Glc–hex-DToc can be considered good candidates for fabricating templates with ultrasmall 3D structures in their thin films.

Subsequently, to further modulate the self-assembly behavior of the glucose–tocopherol BCO, the impact of the chemical nature of the glucose–tocopherol junction was investigated. For this purpose, 6-azidohexanoic acid was replaced with 4-azidobenzoic acid as a linker to impart the BCO with a more rigid chemical junction between the constituent blocks. In this case, 4-azidobenzoic acid was reacted with DL-α-tocopherol and d-α-tocopherol to produce azido-functionalized precursors, which were then subjected to a click reaction with Glc-C≡CH to produce Glc-bz-DLToc and Glc-bz-DToc, respectively (Scheme 1).

No obvious scattering peaks were observed in the WAXS profiles of Glc-bz-DLToc, regardless of the annealing conditions employed, thereby confirming its amorphous nature (Fig. 9b). In contrast, scattering peaks attributed to various microphase-separated structures were detected in the SAXS profiles (Fig. 9a). Interestingly, although both Glc–hex-DLToc and Glc–hex-DToc formed HPL_{ABC} only at lower temperatures (i.e., in the as-cast sample and the sample annealed at 80 °C) and exhibited GYR structures at higher temperatures (i.e., after annealing at 130 and 160 °C), the HPL_{ABC} structure was observed in Glc-bz-DLToc even at elevated temperatures (as-synthesized: a = 10.6 and c = 20.8 nm; annealed at 80 °C: a = 10.2 and c = 17.2 nm; annealed at 130 °C: a = 10.8 and c = 17.9 nm). Furthermore, Glc-bz-DLToc exhibited a hexagonally close-packed cylinders (HEX) structure even after annealing at higher temperatures (annealed at 180 °C: cylinder-to-cylinder distance (d_{c-c}) = 7.5 nm; annealed at 210 °C: d_{c-c} = 7.2 nm). These results clearly demonstrate the significant impact of the linker structure on microphase separation. More specifically, the effect of the linker structure was clearly manifested by the different morphologies of the samples annealed at 130 °C, wherein Glc–hex-DLToc formed a GYR structure, and Glc-bz-DLToc formed an HPL structure. This result implies that the replacement of hexanoate with a benzoate linker reduced the packing parameter of the BCO, thereby enhancing the stability of the lower-curvature HPL phase relative to that of the GYR phase.

It should be noted here that the hexanoate and benzoate linkers consist of an aliphatic pentyl group and an aromatic phenylene ring, respectively. For the first-order approximation, the contribution of these two groups to the hydrocarbon volume

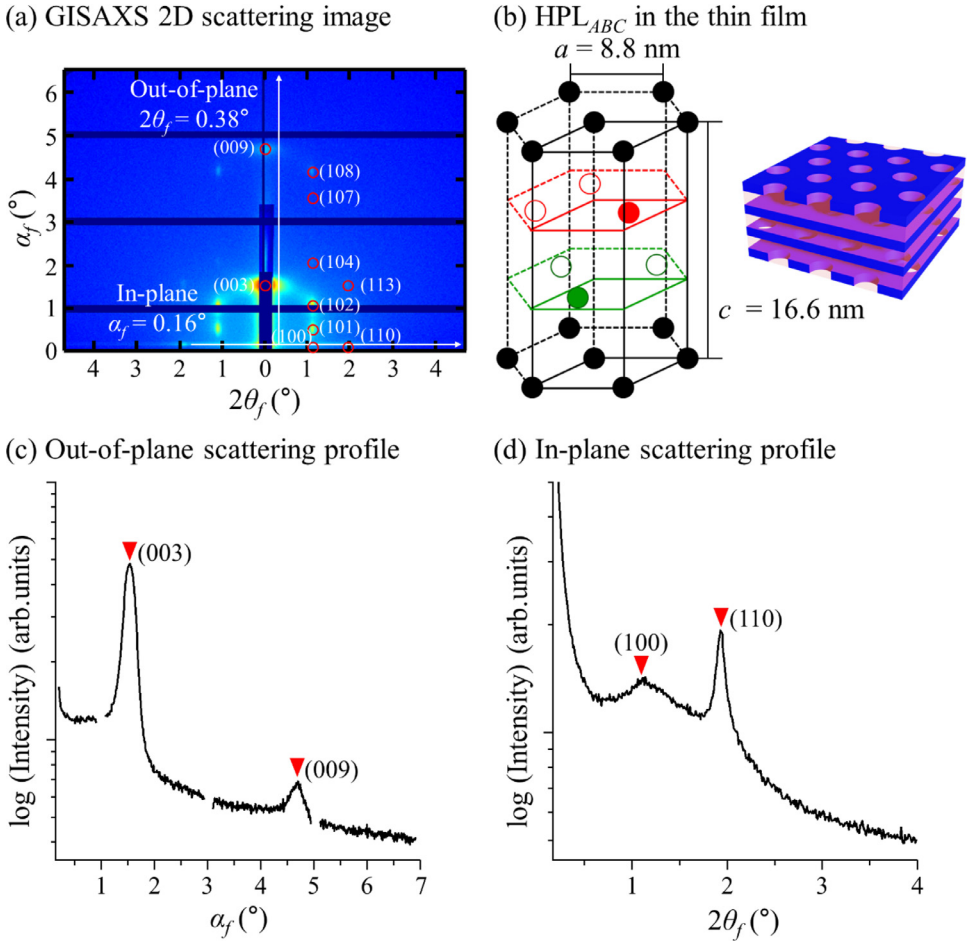

Fig. 8

(a) Representative GISAXS 2D scattering image of the as-cast nanoscale Glc–hex-DToc film (40–50 nm thick) with $\alpha_i = 0.1562°$, SDD = 1024.29 mm, and $\lambda = 1.50$ Å. (b) Schematic illustrations showing the HPL_{ABC} structure. (c) 1D out-of-plane scattering profile along the meridian line at $2\theta_f = 0.38°$, as derived from (a). (d) 1D in-plane scattering profile along the equatorial line at $\alpha_f = 0.16°$, as derived from (a).

of the hydrophobic block was estimated using the ratio of their mass to the corresponding mass density. Taking the values of the mass density ρ as 0.626 g cm^{-3} for pentane and 0.876 g cm^{-3} for benzene, the volumes of the pentylene and phenylene moieties were estimated to be 0.21 and 0.14 nm^3, respectively. Consequently, the replacement of hexanoate with benzoate in the linker reduced the hydrocarbon volume and the packing parameter of the hydrophobic block, such that the thermodynamic stability of the HPL phase in Glc-bz-DLToc was enhanced over that of the GYR phase.

Furthermore, the broad peak observed in the SAXS profiles of the as-synthesized Glc-bz-DToc sample and of the samples annealed at 80 and 130 °C suggested the absence of a periodically ordered structure (Fig. 9c). However, several diffraction peaks were observed in the WAXS profiles of the samples annealed below 130 °C, reflecting the crystallinity of the DToc block (Fig. 9d). The results demonstrate that the crystallization of the DToc block has a strong impact on the microphase-separated structure of the BCO. More specifically, at a lower temperature, the driving force for crystallization could outweigh that of microphase separation, such that the crystallization process perturbs or even disrupts the microphase-separated morphology, leading to a rather disordered structure. Upon annealing at a sufficiently high temperature that exceeds the crystal melting point (i.e., 180 or 210 °C), the driving force for the microphase separation of Glc-bz-DToc led to the formation of well-ordered GYR structures (a_{GYR} = 13.8 and 13.7 nm for the samples annealed at 180 and 210 °C, respectively) (Fig. 9c). It is important to note that different morphologies were observed between Glc-bz-DLToc and Glc-bz-DToc at these two annealing temperatures, wherein the racemic and chiral BCO displayed HEX and GYR structures, respectively, demonstrating that the chirality of tocopherol has a strong influence on the self-assembly behavior in Glc-bz-Toc. However, such a significant effect was not observed for the Glc–hex-Toc specimen bearing a hexanoate linker. This implies that a rigid benzoate linker may amplify the chirality of the tocopherol block. The detailed mechanism underlying this interesting phenomenon, which may be thermodynamic or kinetic in origin, is currently under investigation, and will be reported in due course.

Finally, we investigated the thin film morphologies of Glc-bz-DLToc and Glc-bz-DToc using GISAXS measurements. Although Glc-bz-DLToc and Glc-bz-DToc formed different morphologies in

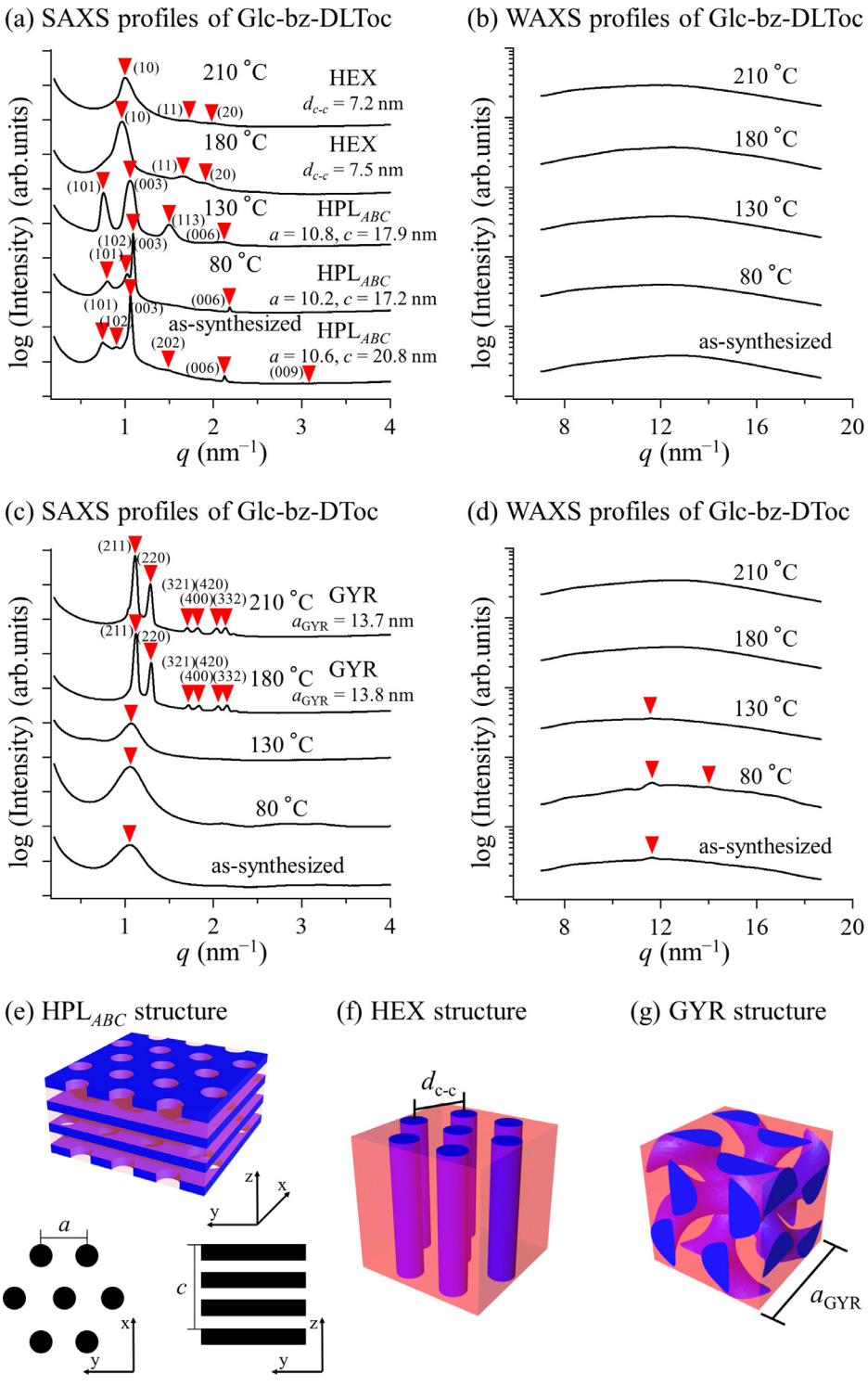

Fig. 9

(a, c) SAXS and (b, d) WAXS profiles of the as-synthesized and thermally annealed Glc-bz-DLToc and Glc-bz-DToc specimens. Schematic illustrations for the (e) HPL$_{ABC}$, (f) HEX, and (g) GYR structures are also provided.

the bulk, both thin films showed a similar self-assembly behavior. More specifically, the as-cast thin films formed horizontally oriented LAM structures (d = 5.4–6.2 nm), while the HPL$_{ABC}$ (a = 9.0–13.3, c = 17.2–18.7 nm) and GYR morphologies (a_{GYR} = 13.9–14.7 nm) were observed upon the thermal annealing at 130–180 °C for 6 h, respectively (**Figures S18,19**). Notably, the GYR structure was obtained from both Glc-bz-DLToc and Glc-bz-DToc thin films even after thermal annealing at 210 °C (Figs. 10a,b), which differs from the results obtained for the bulk sample. Indeed, these results demonstrated that the Glc-bz-

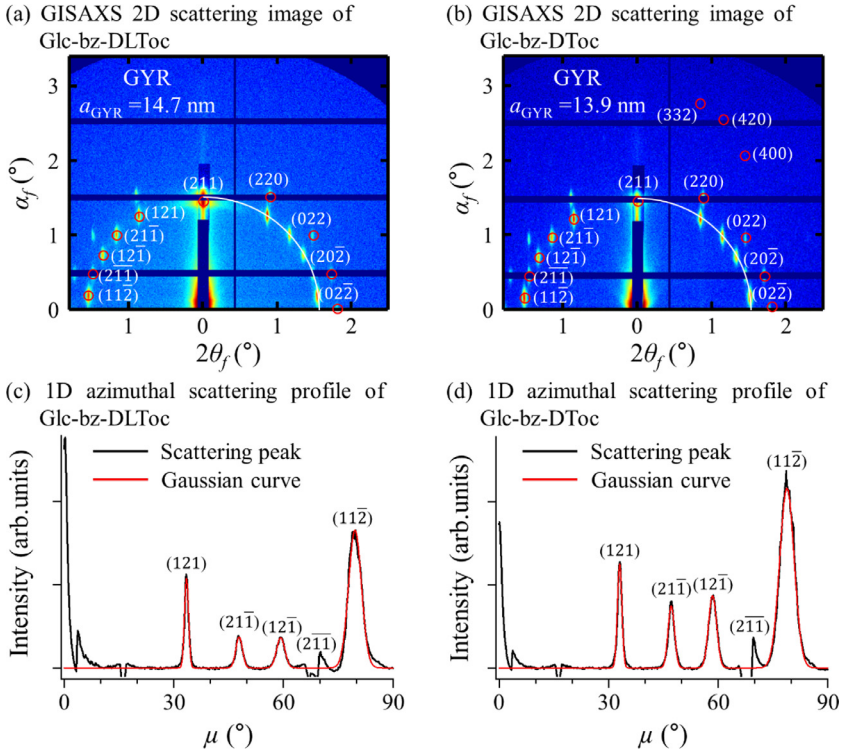

Fig. 10

Representative GISAXS 2D scattering image of the nanoscale (a) Glc-bz-DLToc ($\alpha_i = 0.1062°$) and (b) Glc-bz-DToc ($\alpha_i = 0.1013°$) films (40–50 nm thick) annealed at 210 °C, where SDD = 1024.29 mm and $\lambda = 1.50$ Å. (c, d) The 1D azimuthal scattering profiles at $\alpha_f = 1.44$ and 1.42° (black) and their Gaussian fit curves (red), as determined from (a) and (b), respectively.

DLToc species annealed at 210 °C formed a HEX structure in the bulk state. Interestingly, by comparing the GISAXS 2D scattering images of the Glc-bz-DLToc and Glc-bz-DToc thin films annealed at 210 °C, it was revealed that the optically pure Glc-bz-DToc formed more orderly HPL_{ABC} and GYR structures than the Glc-bz-DLToc specimen, as evidenced by the presence of higher-order scattering spots (e.g., (332), (420), and (400) peaks). Furthermore, 1D azimuthal scattering profiles, which were extracted from the GISAXS 2D scattering images of Glc-bz-DLToc and Glc-bz-DToc, gave α_f values of 1.44 and 1.42°, respectively. The peak intensity and sharpness of each Gaussian fit curve demonstrated that Glc-bz-DToc exhibited a highly ordered GYR structure (Fig. 10c and d), again confirming the positive effects of the tocopherol chirality on the arrangement of the nanostructure.

Conclusion

Ultrafine three-dimensional (3D) network morphologies (i.e., gyroid (GYR) and *ABC*-stacked hexagonally perforated lamellae (HPL_{ABC})), were successfully prepared from biobased sugar–terpenoid hybrid block co-oligomers (BCOs) consisting of glucose and tocopherol. After carrying out small-angle X-ray scattering (SAXS) measurements for a series of BCOs possessing different terpenoids, it became apparent that tocopherol is critical for ensuring the formation of a network morphology, while the other terpenoids, namely farnesol and phytol, resulted in the generation of lamellar structures. These differences can be attributed to the molecular shapes of the corresponding tocopherols, along with the different volume fractions when combined with glucose. Importantly, the HPL_{ABC} and GYR structures were successfully obtained from BCOs consisting of glucose and tocopherol, even in the thin film state. The HPL_{ABC} structure, which is otherwise known as a metastable phase in block copolymers, was maintained even after prolonged high-temperature annealing at 180 °C in the thin film state, thereby confirming the utility of this system as a template for fabricating 3D network nanostructures. Furthermore, it was found that the stereochemistry of the tocopherol hydrocarbon chain affects the microphase separation behavior. Currently studies in our group are focusing on the chirality effects in more detail, and the results will be presented in due course. Finally, the effects of the chemical structure of the bridging linker between the constituent blocks were examined, and it was deduced that a rigid benzoate linker amplified the chirality effect of the hydrocarbon chain, leading to different morphologies. The insights obtained in this study are expected to greatly contribute to the molecular design of precise block copolymers and the construction of intricate nanostructural templates with ultrasmall feature sizes.

Funding sources

This work was financially supported by a JSPS Grant-in-Aid for Scientific Research (No. 20H02792), a JSPS Fund for the Promotion of Joint International Research (No. 21KK0096), the Asahi Glass Foundation, the Photoexcitonix Project (Hokkaido University), the Project of Junior Scientist Promotion at Hokkaido University,

and the Creative Research Institute (Hokkaido University). This study was approved by the Photon Factory Program Advisory Committee (Proposal Nos. 2021G0531 and 2020G649).

Declaration of Competing Interest

The authors declare that they have no known competing financial interests or personal relationships that could have appeared to influence the work reported in this paper.

Data availability

Data will be made available on request.

Supplementary materials

Supplementary material associated with this article can be found, in the online version, at doi:10.1016/j.giant.2023.100211.

References

[1] M.P. Stoykovich, P.F. Nealey, Block copolymers and conventional lithography, Mater. Today 9 (2006) 20–29.

[2] M. De La Olvera Cruz, Theory of microphase separation in block copolymer solutions, J. Chem. Phys. 90 (1989) 1995–2002.

[3] F.S. Bates, G.H. Fredrickson, Block copolymers-designer soft materials, Phys. Today 52 (1999) 32–38.

[4] F.S. Bates, H.E. Bair, M.A. Hartney, Block Copolymers near the microphase separation transition. 1. Preparation and physical characterization of a model system, Macromolecules 17 (1984) 1987–1993.

[5] X. Li, C. Wang, J. Zhou, Z. Yang, Y. Zhang, H. Deng, Ultra-fast block copolymers for sub-5nm lithographic patterning, J. Photopolym. Sci. Technol. 31 (2018) 483–486.

[6] S. Ji, L. Wan, C.C. Liu, P.F. Nealey, Directed self-assembly of block copolymers on chemical patterns: a platform for nanofabrication, Prog. Polym. Sci. 54–55 (2016) 76–127.

[7] Y. Shao, B. Hou, W. Li, X. Yan, X. Wang, Y. Xu, Q. Dong, W. Li, J. He, W.Bin Zhang, Three-Component Bolaform Giant Surfactants Forming Lamellar Nanopatterns with Sub-5nm Feature Sizes, Macromolecules 56 (2023) 1562–1571.

[8] B. Hou, W.B. Zhang, Y. Shao, Unconventional 2D periodic nanopatterns based on block molecules, Chinese J. Polym. Sci. 41 (2023) 1508–1524.

[9] J. Oh, H.S. Suh, Y. Ko, Y. Nah, J.C. Lee, B. Yeom, K. Char, C.A. Ross, J.G. Son, Universal perpendicular orientation of block copolymer microdomains using a filtered plasma, Nat. Commun. 10 (2019) 2912.

[10] W.A. Phillip, B. O'Neill, M. Rodwogin, M.A. Hillmyer, E.L. Cussler, Self-assembled block copolymer thin films as water filtration membranes, ACS Appl. Mater. Interfaces 2 (2010) 847–853.

[11] E.W. Cochran, C.J. Garcia-Cervera, G.H. Fredrickson, Stability of the gyroid phase in diblock copolymers at strong segregation, Macromolecules 39 (2006) 4264.

[12] D.A. Hajduk, P.E. Harper, S.M. Gruner, C.C. Honeker, G. Kim, E.L. Thomas, L.J. Fetters, The gyroid: a new equilibrium morphology in weakly segregated diblock copolymers, Macromolecules 27 (2002) 4063–4075.

[13] H. Wu, H. Huang, Y. Zhang, X. Lu, P.W. Majewski, X. Feng, Stabilizing differential interfacial curvatures by mismatched molecular geometries: toward polymers with percolating 1nm channels of gyroid minimal surfaces, ACS Nano 16 (2022) 21139–21151.

[14] C.H. Hsu, K. Yue, J. Wang, X.H. Dong, Y. Xia, Z. Jiang, E.L. Thomas, S.Z.D. Cheng, Thickness-dependent order-to-order transitions of bolaform-like giant surfactant in thin films, Macromolecules 50 (2017) 7282–7290.

[15] W. Shan, W. Zhang, M. Huang, Y. Ji, R. Zhang, R. Zhang, Z. Su, H. Liu, X. Feng, D. Guo, J. Huang, T. Liu, T. Li, J. Mao, C. Wesdemiotis, A.C. Shi, S.Z.D. Cheng, Fine-tuned order-order phase transitions in giant surfactants via interfacial engineering, Giant 1 (2020) 100002.

[16] P.G. Khalatur, A.R. Khokhlov, Nonconventional scenarios of polymer self-assembly, Soft Matter 9 (2013) 10943–10954.

[17] E.L. Thomas, D.B. Alward, D.J. Kinning, D.C. Martin, D.L. Handlin Jr, L.J. Fetters, Ordered bicontinuous double-diamond structure of star block copolymers: a new equilibrium microdomain morphology, Macromolecules 19 (2002) 2197–2202.

[18] A.E. Likhtman, A.N. Semenov, Stability of the OBDD structure for diblock copolymer melts in the strong segregation limit, Macromolecules 27 (2002) 3103–3106.

[19] W. Takagi, J. Suzuki, Y. Aoyama, T. Mihira, A. Takano, Y. Matsushita, Bicontinuous double-diamond structures formed in ternary blends of AB diblock copolymers with block chains of different lengths, Macromolecules 52 (2019) 6633–6640.

[20] C.Y. Chu, X. Jiang, H. Jinnai, R.Y. Pei, W.F. Lin, J.C. Tsai, H.L. Chen, Real-space evidence of the equilibrium ordered bicontinuous double diamond structure of a diblock copolymer, Soft Matter 11 (2015) 1871–1876.

[21] I. Vukovic, G. Ten Brinke, K. Loos, Hexagonally perforated layer morphology in PS-b-P4VP(PDP) supramolecules, Macromolecules 45 (2012) 9409–9418.

[22] T. Wen, H.F. Wang, P. Georgopanos, A. Avgeropoulos, R.M. Ho, Three-dimensional visualization of phase transition in polystyrene-block-polydimethylsiloxane thin film, Polymer (Guildf) 167 (2019) 209–214.

[23] M.W. Matsen, F.S. Bates, Unifying weak- and strong-segregation block copolymer theories, Macromolecules 29 (1996) 1091–1098.

[24] M.W. Matsen, F.S. Bates, Origins of complex self-assembly in block copolymers, Macromolecules 29 (1996) 7641–7644.

[25] A. Mukherjee, K. Ankit, A. Reiter, M. Selzer, B. Nestler, Electric-field-induced lamellar to hexagonally perforated lamellar transition in diblock copolymer thin films: kinetic pathways, Phys. Chem. Chem. Phys. 18 (2016) 25609–25620.

[26] J. Jung, H.W. Park, J. Lee, H. Huang, T. Chang, Y. Rho, M. Ree, H. Sugimori, H. Jinnai, Structural characterization of the Fddd phase in a diblock copolymer thin film by electron microtomography, Soft Matter 7 (2011) 10424–10428.

[27] Y.C. Wang, M. Im Kim, S. Akasaka, K. Saijo, H. Hasegawa, T. Hikima, M. Takenaka, Fddd structure in polystyrene-block-polyisoprene diblock copolymer/polystyrene homopolymer blends, Macromolecules 49 (2016) 2257–2261.

[28] V.N. Urade, T.C. Wei, M.P. Tate, J.D. Kowalski, H.W. Hillhouse, Nanofabrication of double-gyroid thin films, Chem. Mater. 19 (2007) 768–777.

[29] K. Yamada, M. Nonomura, T. Ohta, *Fddd* structure in AB-type diblock copolymers, J. Phys. Condens. Matter 18 (2006) L421–L427.

[30] K.C. Yang, C.T. Yao, L.Y. Huang, J.C. Tsai, W.S. Hung, H.Y. Hsueh, R.M. Ho, Single gyroid-structured metallic nanoporous spheres fabricated from double gyroid-forming block copolymers via templated electroless plating, NPG Asia Mater 11 (2019) 9.

[31] M. González-Castaño, F. Baena-Moreno, J.Carlos Navarro de Miguel, K.U.M. Miah, F. Arroyo-Torralvo, R. Ossenbrink, J.A. Odriozola, W. Benzinger, A. Hensel, A. Wenka, H. Arellano-García, 3D-printed structured catalysts for CO_2 methanation reaction: advancing of gyroid-based geometries, Energy Convers. Manag 258 (2022) 115464.

[32] L. Li, L. Schulte, L.D. Clausen, K.M. Hansen, G.E. Jonsson, S. Ndoni, Gyroid nanoporous membranes with tunable permeability, ACS Nano 5 (2011) 7754–7766.

[33] L. Li, P. Szewczykowski, L.D. Clausen, K.M. Hansen, G.E. Jonsson, S. Ndoni, Ultrafiltration by gyroid nanoporous polymer membranes, J. Memb. Sci. 384 (2011) 126–135.

[34] S. Zheng, M.C. Hoang, V. Du Nguyen, G. Go, M. Nan, B.A. Darmawan, S. Kim, S.H. Im, T. Lee, D. Bang, J.O. Park, E. Choi, Microrobot with gyroid surface and gold nanostar for high drug loading and near-infrared-triggered chemo-photothermal therapy, Pharmaceutics 14 (2022).

[35] H.C. Lee, H.Y. Hsueh, U.S. Jeng, R.M. Ho, Functionalized nanoporous gyroid SiO2 with double-stimuli- responsive properties as environment-selective delivery systems, Macromolecules 47 (2014) 3041–3051.

[36] J.O. Tella, J.A. Adekoya, K.O. Ajanaku, Mesoporous silica nanocarriers as drug delivery systems for anti-tubercular agents: a review, R. Soc. Open Sci. 9 (2022) 6.

[37] A.M. Urbas, M. Maldovan, P. DeRege, E.L. Thomas, Bicontinuous cubic block copolymer photonic crystals, Adv. Mater. 14 (2002) 1850–1853.

[38] S. Peng, R. Zhang, V.H. Chen, E.T. Khabiboulline, P. Braun, H.A. Atwater, Three-dimensional single gyroid photonic crystals with a mid-infrared bandgap, ACS Photonics 3 (2016) 1131–1137.

[39] M. Fruchart, S.Y. Jeon, K. Hur, V. Cheianov, U. Wiesner, V. Vitelli, Soft self-assembly of Weyl materials for light and sound, Proc. Natl. Acad. Sci. U. S. A. 115 (2018) E3655–E3664.

[40] E.J.W. Crossland, M. Kamperman, M. Nedelcu, C. Ducati, U. Wiesner, D.M. Smilgies, G.E.S. Toombes, M.A. Hillmyer, S. Ludwigs, U. Steiner, H.J. Snaith, A bicontinuous double gyroid hybrid solar cell, Nano Lett 9 (2008) 2807–2812.

[41] A.S. Zalusky, R. Olayo-Valles, C.J. Taylor, M.A. Hillmyer, Mesoporous polystyrene monoliths, J. Am. Chem. Soc. 123 (2001) 1519–1520.

[42] X.B. Wang, T.Y. Lo, H.Y. Hsueh, R.M. Ho, Double and single network phases in polystyrene-block-poly(l-lactide) diblock copolymers, Macromolecules 46 (2013) 2997–3004.

[43] H.M.G. Barriga, M.N. Holme, M.M. Stevens, Cubosomes: the next generation of smart lipid nanoparticles? Angew. Chemie. Int. Ed. 58 (2019) 2958–2978.

[44] W.I. Park, Y. Kim, J.W. Jeong, K. Kim, J.K. Yoo, Y.H. Hur, J.M. Kim, E.L. Thomas, A. Alexander-Katz, Y.S. Jung, Host-guest self-assembly in block copolymer blends, Sci. Rep. 3 (2013) 1–10.

[45] A.K. Khandpur, S. Förster, F.S. Bates, I.W. Hamley, A.J. Ryan, W. Bras, K. Almdal, K. Mortensen, Polyisoprene-polystyrene diblock copolymer phase diagram near the order-disorder transition, Macromolecules 28 (1995) 8796–8806.

[46] C.H. Lin, T. Higuchi, H.L. Chen, J.C. Tsai, H. Jinnai, T. Hashimoto, Stabilizing the ordered bicontinuous double diamond structure of diblock copolymer by configurational regularity, Macromolecules 51 (2018) 4049–4058.

[47] S.P. Ding, Z.K. Zhang, Z. Ye, B.Y. Du, J.T. Xu, Fabrication of high χ-low N block copolymers with thermally stable sub-5nm microdomains using polyzwitterion as a constituent block, ACS Macro Lett 10 (2021) 1321–1325.

[48] S.M. Park, X. Liang, B.D. Harteneck, T.E. Pick, N. Hiroshiba, Y. Wu, B.A. Helms, D.L. Olynick, Sub-10nm nanofabrication via nanoimprint directed self-assembly of block copolymers, ACS Nano 5 (2011) 8523–8531.

[49] C. Sinturel, F.S. Bates, M.A. Hillmyer, High χ–low N block polymers: how far can we go? ACS Macro Lett 4 (2015) 1044–1050.

[50] Z. Shen, K. Luo, S.Jung Park, D. Li, M.K. Mahanthappa, F.S. Bates, K.D. Dorfman, T.P. Lodge, J.Ilja Siepmann, Stabilizing a double gyroid network phase with 2nm feature size by blending of lamellar and cylindrical forming block oligomers, JACS Au 2 (2022) 1405–1416.

[51] S.R. Nowak, K.K. Lachmayr, K.G. Yager, L.R. Sita, Stable thermotropic 3D and 2D double gyroid nanostructures with sub-2-nm feature size from scalable sugar–polyolefin conjugates, Angew. Chemie. Int. Ed. 60 (2021) 8710–8716.

[52] X. Yu, K. Yue, F. Hsieh, Y. Li, X.H. Dong, C. Liu, Y. Xin, H.F. Wang, A.C. Shi, G.R. Newkome, R.M. Ho, E.Q. Chen, W. Bin Zhang, S.Z.D. Cheng, Giant surfactants provide a versatile platform for sub-10-nm nanostructure engineering, Proc. Natl. Acad. Sci. U. S. A. 110 (2013) 10078–10083.

[53] X. Cai, S. Hauche, S. Poppe, Y. Cao, L. Zhang, C. Huang, C. Tschierske, F. Liu, Network phases with multiple-junction geometries at the gyroid-diamond transition, J. Am. Chem. Soc. 145 (2023) 1000–1010.

[54] T. Isono, R. Komaki, C. Lee, N. Kawakami, B.J. Ree, K. Watanabe, K. Yoshida, H. Mamiya, T. Yamamoto, R. Borsali, K. Tajima, T. Satoh, Rapid access to discrete and monodisperse block co-oligomers from sugar and terpenoid toward ultrasmall periodic nanostructures, Commun. Chem. 3 (2020) 1–9.

[55] R. Hashim, N.I. Zahid, T.S. Velayutham, N.F.K. Aripin, S. Ogawa, A. Sugimura, Dry thermotropic glycolipid self-assembly: a review, J. Oleo Sci. 67 (2018) 651–668.

[56] H.M. Von Minden, K. Brandenburg, U. Seydel, M.H.J. Koch, V. Garamus, R. Willumeit, V. Vill, Thermotropic and lyotropic properties of long chain alkyl glycopyranosides. Part II. Disaccharide headgroups, Chem. Phys. Lipids 106 (2000) 157–179.

[57] T. Isono, R. Komaki, N. Kawakami, K. Chen, H.L. Chen, C. Lee, K. Suzuki, B.J. Ree, H. Mamiya, T. Yamamoto, R. Borsali, K. Tajima, T. Satoh, Tailored solid-state carbohydrate nanostructures based on star-shaped discrete block co-oligomers, Biomacromolecules 23 (2022) 3978–3989.

[58] J.N. Israelachvili, *Intermolecular and Surface Forces: third Edition* (2011).

[59] S. Ogawa, K. Asakura, S. Osanai, Lyotropic behavior of a mono-tailed glycolipid assembly during solidification and melting of electrolyte/ice eutectic systems, Chem. Pharm. Bull. 62 (2014) 1180–1184.

[60] O. Misran, B.A. Timimi, T. Heidelberg, A. Sugimura, R. Hashim, Deuterium NMR investigation of the lyotropic phases of alkyl β-glycoside/D2O systems, J. Phys. Chem. B 117 (2013) 7335–7344.

[61] J.M. Seddon, N. Zeb, R.H. Templer, R.N. McElhaney, D.A. Mannock, An Fd3m lyotropic cubic phase in a binary glycolipid/water system, Langmuir 12 (1996) 5250–5253.

[62] P. Garidel, Y. Kaconis, L. Heinbockel, M. Wulf, S. Gerber, A. Munk, V. Vill, K. Brandenburg, Self-Organisation, Thermotropic and Lyotropic Properties of Glycolipids Related to their Biological Implications, Open Biochem. J. 9 (2015) 49–72.

[63] D.A. Mannock, R.N. McElhaney, Thermotropic and lyotropic phase properties of glycolipid diastereomers: role of headgroup and interfacial interactions in determining phase behaviour, Curr. Opin. Colloid Interface Sci. 8 (2004) 426–447.

[64] R.H. Zha, B.F.M. De Waal, M. Lutz, A.J.P. Teunissen, E.W. Meijer, End groups of functionalized siloxane oligomers direct block-copolymeric or liquid-crystalline self-assembly behavior, J. Am. Chem. Soc. 138 (2016) 5693–5698.

[65] V. Vill, H.M. von Minden, M.H.J. Koch, U. Seydel, K. Brandenburg, Thermotropic and lyotropic properties of long chain alkyl glycopyranosides: part I: monosaccharide headgroups, Chem. Phys. Lipids 104 (2000) 75–91.

[66] V. Vill, T. Böcker, J. Thiem, F. Fischer, Studies on liquid-crystalline glycosides, Liq. Cryst 6 (1989) 349–356.

[67] B.J. Boydirc, C.J. Drummond, I. Krodkiewska, F. Grieser, How chain length, headgroup polymerization, and anomeric configuration govern the thermotropic and lyotropic liquid crystalline phase behavior and the air-water interfacial adsorption of glucose-based, Surfactants, Langmuir 16 (2000) 7359–7367.